https://doi.org/10.5194/egusphere-2026-5788
Preprint. Discussion started: 19 October 2026
© Author(s) 2026. CC BY 4.0 License.

Global Hourly Aerosol Optical Depth Retrieval from DSCOVR/EPIC Observation and Its Application in Extreme Wildfire Events

Xiaohu Sun[1], Yong Xue[1], Zhiqiang Cui[2], Wuhu Feng[2], Bingyue Cao[1]

[1]School of Atmospheric Physics, Nanjing University of Information Science and Technology, Nanjing, 210044, China
[2] School of Earth, Environment and Sustainability, University of Leeds, Leeds, LS2 9JT, United Kingdom

Correspondence to: Yong Xue (yxue@nuist.edu.cn), Zhiqiang Cui (Z.Cui@leeds.ac.uk)

Abstract. Extreme wildfire events can substantially perturb the global radiative balance and cause severe transboundary air pollution. Their aerosol plumes evolve rapidly on hourly timescales, yet low Earth orbit satellites have limited revisit frequency, while geostationary satellites have restricted hemispheric coverage. The Earth Polychromatic Imaging Camera (EPIC) aboard NOAA's Deep Space Climate Observatory (DSCOVR), located at the Sun–Earth L1 point, provides continuous observations of the sunlit Earth disk with high temporal and unique aerosol sensitivity from ultraviolet (UV) to oxygen absorption bands. Here, we use an end-to-end deep learning framework for hourly global aerosol optical depth (AOD) retrieval using a parameter-efficient BatchEnsemble-based architecture, enabling efficient large-scale inference and quantitative uncertainty estimation. The framework integrates multispectral across UV, visible, and O_2 A/B bands with meteorological and topographic information. Against AERONET observations, the retrieval achieves R = 0.909, InEE = 90.91%, MAE = 0.039, and RMSE = 0.066 in sample-based validation, and maintaining robust performance under spatial and interannual extrapolation, with InEE consistently exceeding 74%. SHAP analysis reveals physically meaningful feature contributions, with UV bands contributing 58.9%, followed by visible bands (18.7%), spatiotemporal features (10.0%), meteorological parameters (6.7%), and O_2 A/B bands (4.7%). The retrieval also outperforms operational EPIC products and provides substantially more valid retrievals. Case studies over Canada, Australia, and the western United States demonstrate the retrieved hourly AOD captures the intraday evolution and long-range transport of wildfire smoke. These results highlight the potential of DSCOVR/EPIC and deep learning for continuous global monitoring of rapidly evolving aerosol events.

1. Introduction

In recent years, extreme wildfire events have become increasingly frequent, intense, and long-lasting (Li et al., 2021; Torres et al., 2025; Deng et al., 2026). These fires emit large quantities of aerosol, significantly perturbing the global radiation balance and causing severe air pollution (Ansmann et al., 2021; Wei et al., 2023). These aerosol events are characterized by their striking suddenness and high temporal variability, with smoke plume trajectories changing dramatically on hourly timescales

https://doi.org/10.5194/egusphere-2026-5788
Preprint. Discussion started: 19 October 2026
© Author(s) 2026. CC BY 4.0 License.

(Torres et al., 2025). Consequently, the high-frequency, large-scale monitoring of aerosol optical depth (AOD) is of great significance.

Low Earth Orbit (LEO) satellites play a crucial role in aerosol monitoring. Sensors such as the Moderate Resolution Imaging Spectroradiometer (MODIS) aboard Terra and Aqua, and the Visible Infrared Imaging Radiometer Suite (VIIRS) aboard Suomi-NPP, have provided long-term global aerosol records (Hsu et al., 2019; Levy et al., 2010, 2013; Sawyer et al., 2025; Sayer et al., 2014). However, LEO satellites are constrained by long revisit cycles (typically once or twice daily), preventing them from capturing rapid aerosol dynamics and potentially omitting critical processes (Fan et al., 2026). Such sparse temporal sampling can also introduce substantial biases into radiative forcing estimates (Che et al., 2024; Fan et al., 2025a). To achieve continuous time-series observations, Geostationary Earth Orbit (GEO) satellites are widely used for wildfire monitoring (Zhang et al., 2026). Next-generation GEO platforms (e.g., Himawari-8/9 with AHI, MSG with SEVIRI, MTG with FCI, and GOES with ABI) provide sub-hourly observations (Ichii, 2026), greatly improving the tracking of fire outbreaks and smoke plume dispersion. However, the field of view of any single GEO satellite is confined to a fixed hemisphere, meaning that capturing global-scale transport of wildfire smoke requires a multi-satellite constellation.

The Earth Polychromatic Imaging Camera (EPIC) aboard the Deep Space Climate Observatory (DSCOVR), positioned at the Sun–Earth L1 Lagrange point, offers a unique observational perspective (Lu et al., 2023; Marshak et al., 2018). EPIC captures images of the sunlit Earth hemisphere 10 to 22 times daily, combining the global coverage of LEO satellites with the high temporal resolution of GEO platforms. More importantly, EPIC features 10 narrow spectral channels from ultraviolet (UV) to visible and near-infrared (VIS/NIR) wavelengths, providing a basis for retrieving aerosol optical properties. Specifically, the 340 nm and 388 nm bands are sensitive to absorbing carbonaceous aerosols (Ahn et al., 2021), while the low surface reflectance in the UV region enables accurate detection of absorbing smoke over bright surfaces. Additionally, the O2 A/B bands are sensitive to the vertical distribution of aerosols (Chen et al., 2021; de Graaf et al., 2025; Xu et al., 2017, 2019). Because extreme wildfires frequently inject smoke into high altitudes, incorporating these O2 absorption bands can improve the characterization of aerosol vertical profiles and reduces retrieval biases. Due to the lack of shortwave infrared (SWIR) channels and near-backscattering geometry, the official Level 2 AOD products are currently derived using two main approaches: the UV-based algorithm (Ahn et al., 2021; Torres and Ahn, 2024) and the MAIAC-based algorithm (Lyapustin et al., 2021b, a, 2025). In MAIAC Version-3 (Lyapustin et al., 2025), when strongly absorbing smoke or dust is detected (e.g., background AOD > 0.4 or high UVAI), the algorithm replaces its simplified background assumption with a Levenberg-Marquardt optimization scheme, which integrates UV (340, 388 nm), VIS (443, 680 nm), and O2 A/B bands. The retrieval is subsequently executed using a comprehensive look-up table (LUT) covering various aerosol layer heights and absorption levels.

The iterative optimization process based on comprehensive physical principles demonstrates the robustness of traditional algorithms in handling complex aerosol conditions (Sasi et al., 2020). In contrast, deep learning (DL) model provides an alternative way for exploiting multispectral satellite observations. The main advantages of DL-based retrieval can be summarized as follows: (1) An end-to-end architecture transforms computationally intensive iterative retrieval into efficient forward inference, substantially improving the efficiency of large-scale aerosol retrieval; (2) Multi-source meteorological and

https://doi.org/10.5194/egusphere-2026-5788
Preprint. Discussion started: 19 October 2026
© Author(s) 2026. CC BY 4.0 License.

environmental variables can be integrated as input features, enabling more comprehensive characterization of aerosol variability; (3) Without relying on predefined surface reflectance or aerosol models, DL directly learns complex nonlinear relationships between satellite observations and AOD, thereby reducing retrieval uncertainties associated with physical parameterization assumptions (Tian et al., 2024; Yao et al., 2026).

This study employs a deep learning framework integrated with multi-source data to fully leverage the high-frequency observations and rich multispectral capabilities of DSCOVR EPIC. By incorporating critical channels absent from current LEO and GEO sensors (such as UV and O2 A/B bands). Using this framework, we produce a continuous, global, hourly AOD dataset and analyze major extreme wildfire events from 2020 and 2023. The remainder of this study is organized as follows: Section 2 describes the data; Section 3 presents the data processing and model architecture; Sections 4 and 5 provide validation results and three representative case studies; and Section 6 concludes the study.

2. Materials

2.1 DSCOVR EPIC

The Deep Space Climate Observatory (DSCOVR) was launched in February 2015 and positioned at the Sun–Earth L1 Lagrange point, approximately 1.5 million km from Earth (Marshak et al., 2018). This unique orbital configuration enables continuous observation of Earth's entire sunlit hemisphere. The onboard Earth Polychromatic Imaging Camera (EPIC) features ten narrowband channels from the ultraviolet (UV) to near-infrared (NIR), centered at 317, 325, 340, 388, 443, 551, 680, 688, 764, and 779 nm. The instrument employs a 2048 × 2048 pixel charge-coupled device (CCD) detector. The 443 nm channel provides a nadir spatial resolution of approximately 8 km, whereas the remaining channels employ onboard 2 × 2 pixel aggregation for data transmission, yielding a nadir spatial resolution of approximately 16 km. Depending on seasonal conditions and orbital geometry, EPIC acquires 10–22 full-disk observations daily. This study utilizes EPIC Level-1B data, including all ten spectral channels and their associated geometric information. In addition, the Level-2 cloud mask product is used to identify and remove cloud-contaminated pixels.

2.2 AERONET

The Aerosol Robotic Network (AERONET) is a global ground-based aerosol remote sensing network (Holben et al., 1998). Equipped with instruments such as the CE-318 sun–sky radiometer, AERONET provides long-term, continuous, and high-quality observations of aerosol optical and microphysical properties (Dubovik and King, 2000). Aerosol properties are retrieved through direct measurements of solar radiation attenuation and are minimally affected by surface reflectance. Owing to its extremely low AOD uncertainty (typically 0.01–0.02) (Giles et al., 2019), AERONET observations are widely regarded as the ground reference for evaluating satellite aerosol retrieval products. This study uses quality-assured AERONET Level 2.0 observations for model training and independent validation. Since AERONET does not directly provide AOD at 550 nm, a quadratic polynomial interpolation was employed to estimate AOD at 550 nm, as described in Eq. (1).

https://doi.org/10.5194/egusphere-2026-5788
Preprint. Discussion started: 19 October 2026
© Author(s) 2026. CC BY 4.0 License.

$$\log(\tau_\lambda) = a_0 + a_1\log(\lambda) + a_2\log(\lambda)^2 \ , \quad (1)$$

where τ_λ represents the AOD at wavelength λ, and a_0, a_1, a_2 denote the fitting coefficients.

2.3 Auxiliary data

In addition, digital elevation model data (DEM) and meteorological reanalysis variables were incorporated as auxiliary predictors. Surface elevation directly influences the effective atmospheric column thickness, thereby affecting optical air mass and Rayleigh scattering intensity. Topographic data was obtained from the Global Multi-resolution Terrain Elevation Data 2010 (GMTED2010) dataset (Wang et al., 2024). Given the strong coupling between meteorological conditions and aerosol dynamics, ERA5 reanalysis variables were integrated (10 m u- and v- wind components, surface pressure, planetary boundary layer height, total column ozone, and total column water vapor) (Fan et al., 2026). Finally, four operational global aerosol products (EPIC L2 MAIAC, EPIC L2 UV, MCD19A2CMG, and MERRA-2) were selected for comparative analysis and validation.

3. Methodology

To ensure global retrieval applicability, this study adopts an end-to-end retrieval framework, as illustrated in Fig. 1c. This achievement (Fig. 1) is fundamentally based on the model constructed by the batch ensemble architecture and the data provided by EPIC's unique observation geometry, enabling continuous global monitoring of aerosol dynamic changes from only a single satellite.

https://doi.org/10.5194/egusphere-2026-5788
Preprint. Discussion started: 19 October 2026
© Author(s) 2026. CC BY 4.0 License.

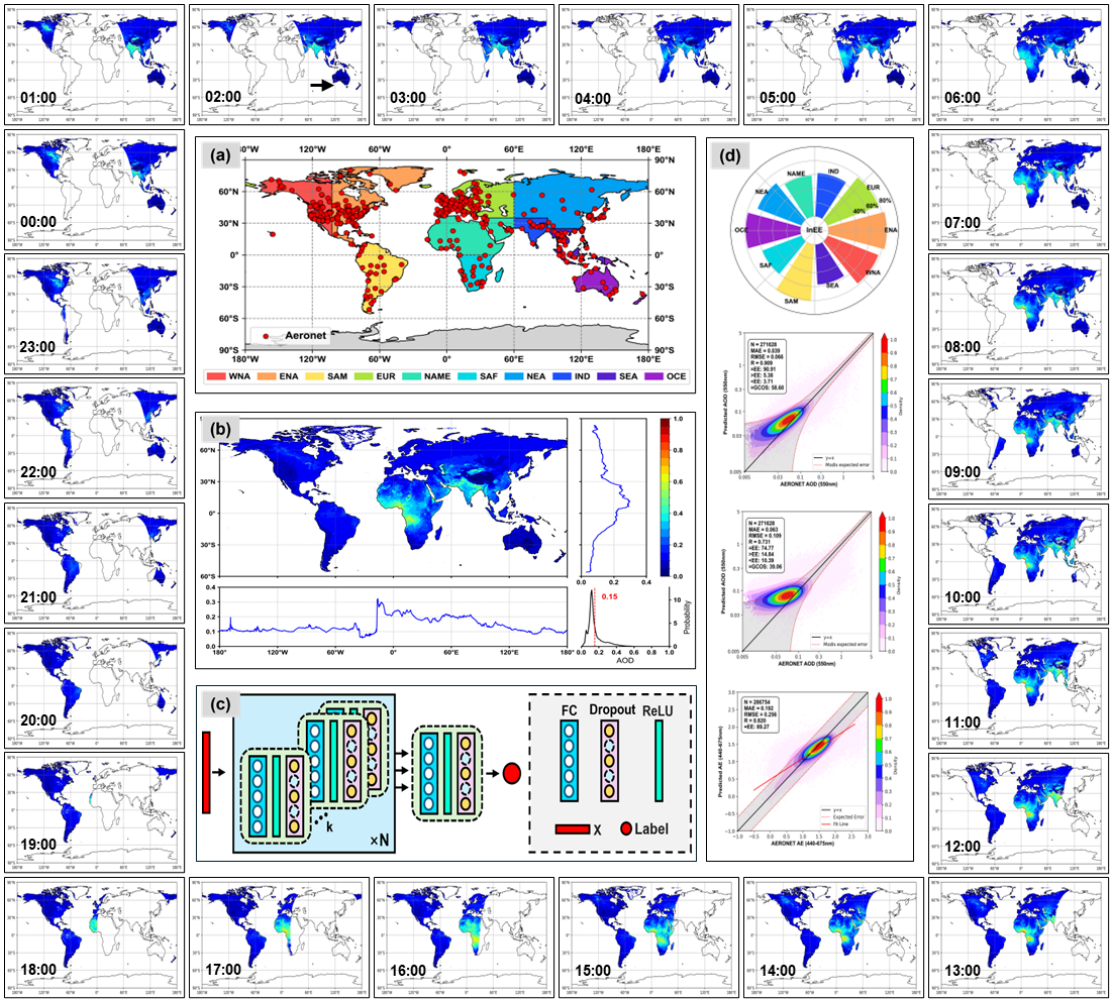


Figure 1. Comprehensive methodological framework for global aerosol retrieval from DSCOVR EPIC observations. The central panels include: (a) spatial distribution of AERONET reference stations, color coded according to ten predefined geographical regions; (b) global mean aerosol optical depth in 2023 by our method; (c) schematic illustration of the deep neural network architecture used for nonlinear aerosol retrieval; and (d) multi-dimensional validation strategies used for model assessment. The outer ring illustrates the continuous hourly observation of the sunlit Earth disk from the L1 point over a complete diurnal cycle (average AOD from 00:00–23:00 UTC in 2023).

3.1 Data processing

In the EPIC Level-1B product, all spectral channels are co-registered within an Earth-centered reference frame. To facilitate time-series analysis on fixed spatial grids and enable dynamic surface characterization, the MAIAC algorithm resamples observations to a 10 km grid in a zonal sinusoidal projection, which minimizes geometric distortion (Lyapustin et al., 2025). Because the deep learning model requires only co-registered spatiotemporal inputs, the EPIC Level-1B are instead resampled directly onto a regular 0.1°×0.1° latitude–longitude grid in this study. The raw Level-1B measurements (counts s^{-1}) are subsequently converted to top-of-atmosphere (TOA) reflectance using the sensor calibration coefficients. A k-d tree search

https://doi.org/10.5194/egusphere-2026-5788
Preprint. Discussion started: 19 October 2026
© Author(s) 2026. CC BY 4.0 License.

coupled with Gaussian-weighted spatial interpolation is employed (Zhang et al., 2025). To account for the convergence of meridians at high latitudes, a local projection correction is incorporated into the distance calculation. Specifically, geographic coordinates are locally projected onto a 2D Cartesian coordinate system, where longitudinal distances are scaled by the cosine of latitude. This transformation preserves physical distances during neighbor searches, thereby improving the accuracy of Gaussian weight assignment. Spatially, reflectance and geometric variables are extracted from EPIC pixels centered on each AERONET site. Temporally, in-situ AOD measurements acquired within ±30 min of the satellite overpass is averaged. To ensure data representativeness, at least two valid AERONET observations are required within this temporal window for each overpass.

3.2 Deep Learning Method

For regression tasks on structured data, gradient boosted decision trees (GBDTs), such as XGBoost and LightGBM, are generally regarded as the benchmark approaches (Qu et al., 2026; Rizkallah, 2025). However, for global-scale, high-frequency retrieval tasks involving hundreds of millions of samples, the substantial memory footprint and relatively slow inference speed of tree-based models pose severe computational bottlenecks. Recently, various DL methods, including Transformer-based architectures (Fan et al., 2025; Sun et al., 2026) and enhanced multilayer perceptron (MLP) networks (Sun et al., 2025; Yan et al., 2026), have substantially improved aerosol retrieval accuracy through architectural and training innovations. Nevertheless, these approaches still face several operational challenges. First, complex attention mechanisms and deep neural network architectures are computationally expensive. Second, single-network models are generally less robust than ensemble methods when modeling complex structured data. Third, most models lack an intrinsic mechanism for estimating predictive uncertainty, which is essential for quality control in satellite products. To balance computational efficiency, predictive capability, and uncertainty quantification, this study adopts the TabM architecture (Gorishniy et al., 2025), an MLP-based model specifically designed for tabular data, as the core backbone for AOD retrieval.

The core of TabM is a parameter-efficient ensemble of MLPs. It leverages BatchEnsemble techniques by combining a shared backbone network with lightweight adaptation layers to emulate multiple sub-models (Wen et al., 2020). Specifically, the architecture replaces conventional fully connected layers with Batch Linear Ensemble layers. Within each hidden layer, all k sub-models share a common weight matrix W, while maintaining only low-dimensional private multiplicative scaling vectors (Ri and Si) and private bias vectors (Bi). The forward propagation process is formulated as:

$$y_i = \left((x \odot R_i)W^T\right) \odot S_i + B_i \ , \quad (2)$$

The TabM architecture offers several advantages for satellite AOD retrieval. First, its shared-backbone design keeps the parameter count comparable to that of a single MLP, enabling efficient scaling and deployment for global scale retrieval. Second, a single forward pass yields k independent predictions. Their mean serves as the final AOD estimate, yielding an ensemble effect that reduces overfitting and improves generalization. Third, the variance across the k predictions can be interpreted as an estimate of retrieval uncertainty.

https://doi.org/10.5194/egusphere-2026-5788
Preprint. Discussion started: 19 October 2026
© Author(s) 2026. CC BY 4.0 License.

In the network configuration (Fig. 1c), the number of ensemble sub-models is set to k = 32, as suggested in the original article (Gorishniy et al., 2025). The backbone network comprises three hidden layers, each with 512 neurons. To enhance robustness and mitigate overfitting, a dropout rate of 0.1 is applied after the ReLU activation function in each hidden layer. At the output stage, a linear ensemble layer assigns independent weight matrices and bias vectors to each sub-model, generating k parallel predictions. During training, the batch size is set to 256 and the initial learning rate is 10-4. Model parameters are optimized using the AdamW optimizer, with mean squared error (MSE) as the loss function. Additionally, an early stopping strategy with a patience of 10 epochs is employed to avoid overtraining and optimize computational efficiency.

3.3 Validation approaches

To comprehensively evaluate model performance, five validation strategies with progressively increasing levels of independence were designed. These include three cross-validation (CV) schemes and two more stringent spatiotemporally independent validation approaches: (1) Sample-based 10-fold CV. All collocated samples are randomly divided into 10 equal subsets. In each iteration, 90% of the data are used for training and the remaining 10% for validation. This procedure is repeated ten times to evaluate the overall model fitting performance. (2) Site-based 10-fold CV. The dataset is randomly partitioned into 10 folds according to the spatial distribution of AERONET sites, evaluating predictive capability at unsampled locations. (3) Time-based CV. Implemented as a 12-fold CV based on calendar months, data from one month are withheld for validation in each iteration while the remaining 11 months serve for training. This strategy is designed to assess the model's ability to capture temporal and seasonal variability. (4) Time-independent validation. Data from 2020 and 2023 are alternately used for training and validation. This temporal extrapolation experiment evaluates model stability and cross-year generalization. (5) Space-independent validation. Based on the geographical zoning shown in Fig. 1a, one region is designated as an independent test set in each iteration, while the remaining regions are used for training. This strategy provides a rigorous assessment of spatial generalization in unseen large-scale regions.

4. Results and Discussion

This section presents and evaluates the AOD retrieval results. Retrieval performance is evaluated using five validation schemes, three comparative benchmarks, and a three-part uncertainty analysis. Additionally, to enhance spatial visualization, AOD values are scaled to the 0-1 range for rendering; this display adjustment is applied strictly for visual clarity and does not affect any quantitative analyses.

4.1 Evaluation and validation of retrieval results

As shown in Fig. 2, the model demonstrates robust stability and strong generalization capability for AOD retrieval. Under the sample-based CV strategy (Fig. 2a), model predictions show strong agreement with AERONET observations (R = 0.909, InEE = 90.91%). More importantly, under spatial extrapolation (site-based CV, Fig. 2b) and temporal extrapolation (time-based CV,

https://doi.org/10.5194/egusphere-2026-5788
Preprint. Discussion started: 19 October 2026
© Author(s) 2026. CC BY 4.0 License.

Fig. 2c), model performance degrades only slightly (R > 0.85 and InEE ≈ 85%), with data points remaining tightly clustered along the 1:1 line. Even under the more stringent space-independent and time-independent tests (Fig. 2d, e), the model maintains strong predictive performance (InEE > 74% and MAE ≈ 0.06). Furthermore, the same validation strategies were applied to the Ångström exponent (AE) to evaluate model performance. AE is derived from the spectral gradient of AOD across wavelengths, so small uncertainties can be amplified during AE estimation. Figure S1 illustrates this effect. Under sample-based CV, the model accurately captures aerosol size characteristics (R = 0.820 and InEE = 89.27%). However, under space- and time-independent validation (Fig. S1d, e), the fitted regression line exhibits a distinct flattening trend, characterized by overestimation at low AE values and underestimation at high AE values. This behavior is common in satellite retrieval and reflects a classic regression-to-the-mean effect. When applied to unseen geographical regions, the lack of local aerosol optical constraints causes the model to converge toward the global statistical mean to minimize prediction risk. Nevertheless, even under these extreme extrapolation scenarios, the model maintains an InEE close to 70%, demonstrating robust predictive capability. As shown in Fig. 2g, the official UV-based algorithm performance poorly (R = 0.458, InEE = 26.45%, and RMSE = 0.299), suffering from severe overestimation and substantial scatter in retrievals (Kim et al., 2025). Note that this comparison is evaluated at approximately 500 nm, close to the target wavelength. Although the EPIC MAIAC algorithm incorporates substantial improvements over the UV-based approach, its performance remains inferior to that reported for LEO platforms (R = 0.387, InEE = 62.44%; Fig. 2h) (Lyapustin et al., 2011; Mhawish et al., 2019; Qin et al., 2021). Due to retrieval failures and algorithmic limitations, the numbers of valid collocated samples for the two physical algorithms (N = 198,004 and N = 147,368) is substantially lower than DL method (N = 271,628). Additionally, the reanalysis product, which assimilates multiple satellite datasets, outperforms the official EPIC satellite products (R = 0.810 and InEE = 86.49%; Fig. 2f), though it still falls short of our retrievals.

https://doi.org/10.5194/egusphere-2026-5788
Preprint. Discussion started: 19 October 2026
© Author(s) 2026. CC BY 4.0 License.

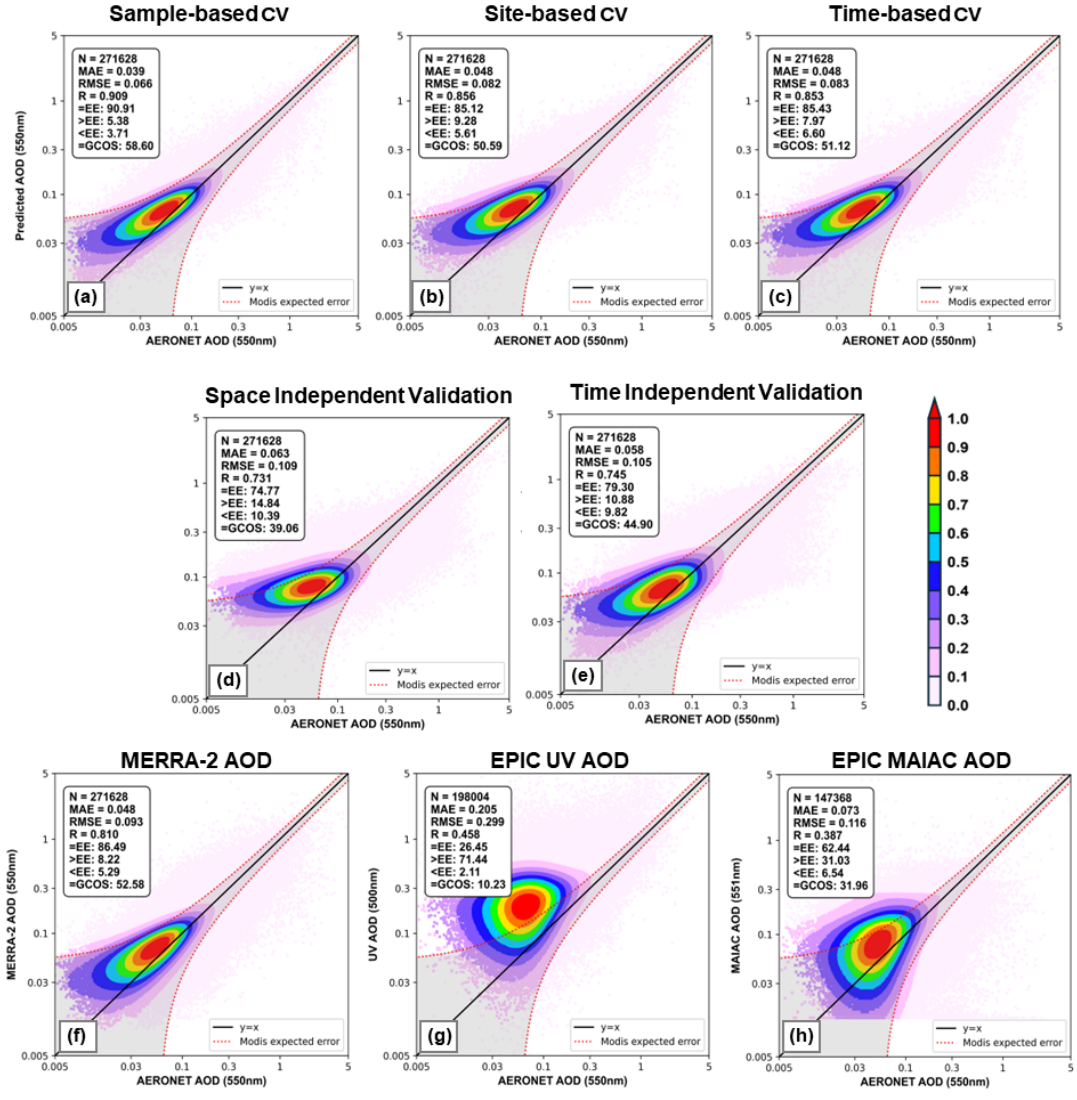


Figure 2. Density scatter plots of retrieved AOD at 550 nm against AERONET ground-based measurements under five evaluation strategies: (a) Sample-based 10-fold cross-validation (CV), (b) Site-based CV, (c) Time-based CV, (d) Space Independent Validation, and (e) Time Independent Validation. Panels (f)–(h) present comparisons with other operational AOD products: (f) MERRA-2 AOD at 550 nm, (g) EPIC UV algorithm AOD at 500 nm, (h) EPIC MAIAC algorithm at 551 nm. The colorbar indicates normalized data point density. The solid black line represents the 1:1 line, while the red dashed lines denote the MODIS Expected Error (InEE) envelope (± (0.05 + 20%τAEROENT)). Note that both axes are plotted on a logarithmic scale to accommodate the wide dynamic range of aerosol loadings.

4.2 Interpretation of Feature Contributions

As shown in Fig. 3, the global feature attribution analysis based on SHAP (SHapley Additive exPlanations) reveals that the model's reliance on input features is highly consistent with physical mechanisms. The ultraviolet (UV) bands, particularly the 388 and 340 nm channels, dominate model predictions with a cumulative contribution of 58.9%. From a radiative transfer

https://doi.org/10.5194/egusphere-2026-5788
Preprint. Discussion started: 19 October 2026
© Author(s) 2026. CC BY 4.0 License.

perspective, this dominance arises because most land surfaces in the UV region can be approximated as low-reflectance "dark targets," thereby enhancing aerosol scattering signatures and providing the model with exceptionally high signal-to-noise ratio information (Li et al., 2025). In contrast, high surface reflectance in the visible (VIS) spectrum often obscures weak aerosol scattering signals. The VIS bands traditionally used in aerosol retrieval rank second in importance, with a total contribution of 18.7%. Among geometric variables, the solar zenith angle (SZA) ranks third in overall importance and exhibits a pronounced directional influence on model predictions. The SHAP dependence plot shows that large SZA values generally contribute negatively to the prediction, whereas smaller SZA values exert a positive influence. This pattern is consistent with the increased retrieval uncertainty observed in off-nadir view geometries (Ceamanos et al., 2023a). Notably, although satellite spectral information (UV and VIS bands) accounts for nearly 80% of the predictive contribution, the model still effectively leverages auxiliary features to further reduce retrieval uncertainties. For example, the O2 A/B absorption bands, which are highly sensitive to the atmospheric optical path length (Xu et al., 2017, 2019), contribute 4.7% to the overall prediction. Additionally, spatiotemporal encoding features (spatial: 6.9%; temporal: 3.1%) and meteorological parameters (6.7%) serve as weak prior constraints, providing useful adjustments that help the model distinguish aerosol regimes across different geographical regions and seasons. This strong alignment between feature importance rankings and radiative transfer principles reinforces confidence in the physical interpretability and generalizability of the proposed deep learning framework.

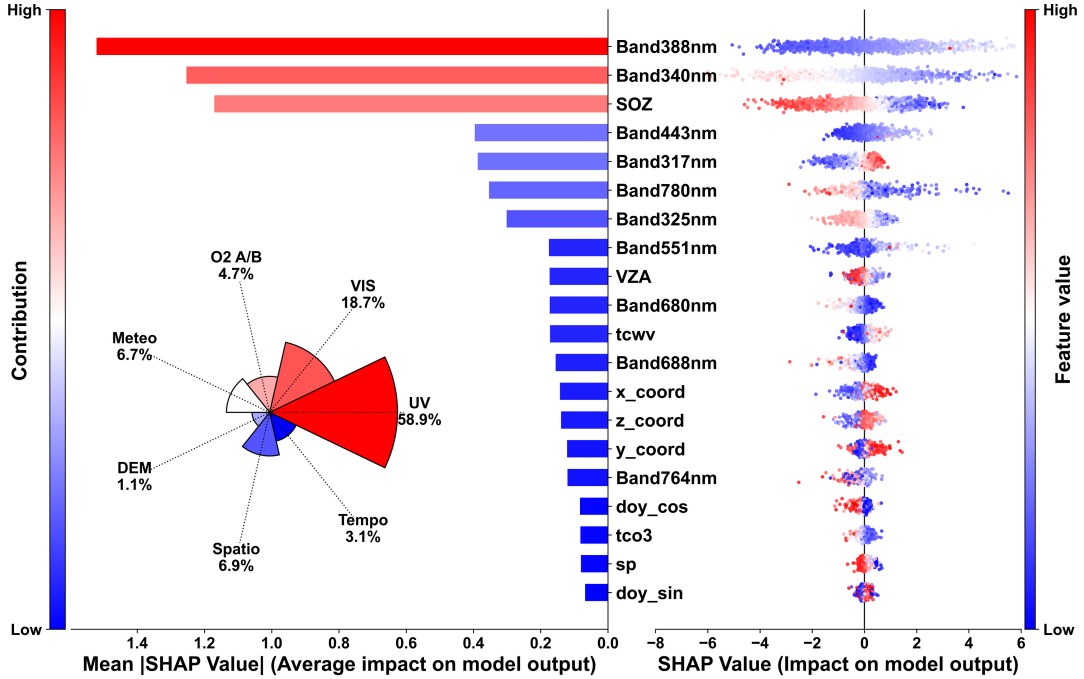


Figure 3. SHAP (SHapley Additive exPlanations) summary plot about the global and local feature contributions to the model. The left panel ranks the input features by their mean absolute SHAP values. The inset polar chart aggregates the relative percentage contributions of different feature categories. The right panel presents a SHAP scatter plot, where each dot represents a single sample. The color indicates the actual feature value (red for high, blue for low), and the position on the x-axis shows the directional impact (positive or negative) of that feature on the model's final output.

https://doi.org/10.5194/egusphere-2026-5788
Preprint. Discussion started: 19 October 2026
© Author(s) 2026. CC BY 4.0 License.

4.3 Evaluation of Spatial Pattern Consistency

Fig. 4 illustrates the continuous full-disk evolution of aerosol optical depth (AOD) across Earth's sunlit hemisphere on 29 August 2023. The unique deep-space viewing of DSCOVR EPIC enables dynamic tracking of rapidly evolving aerosol events at approximately 1-2 h intervals. Fig. 5a presents daily EPIC AOD retrievals, revealing a spatially continuous and globally coherent aerosol distribution pattern. The retrieval successfully captures several key high aerosols loading regions, including extreme wildfire smoke over western Canada, large-scale dust from the Sahara Desert, and biomass-burning emissions over the Amazon. Compared with the MODIS MAIAC product for the same period (Fig. 5b), our retrieval achieves substantially higher spatial coverage and characterize sub-diurnal variability. The spatial distribution of retrieval differences (EPIC − MAIAC) in Fig. 5c further demonstrates the quantitative consistency between two products. Across most global regions, the retrieval results exhibit agreement with MAIAC, with differences close to zero. Specifically, negative differences occur over regions affected by intense wildfire smoke, whereas positive differences emerge over biomass-burning regions in the Amazon. The monthly mean spatial distributions and statistical characteristics of global AOD throughout 2023 (Fig. S5) further reproduce the seasonal variability of major aerosol source regions. For example, dust aerosols over the Sahara and Arabian Peninsula peak during the Northern Hemisphere summer (June-August) (Gandham et al., 2023; Tindan et al., 2025), producing a pronounced mid- to low-latitude maximum in the zonal mean distribution. During the same period, biomass-burning activity in south-central Africa (Wang et al., 2025) and wildfire emissions in Canada are also clearly represented. Additionally, probability density functions reveal that global mean AOD remains relatively stable throughout the year, fluctuating between 0.12 and 0.18 and exhibiting a characteristic long-tailed lognormal distribution. Owing to seasonal variations in solar illumination geometry, substantial observational gaps occur over the high Northern Hemisphere during winter.

https://doi.org/10.5194/egusphere-2026-5788
Preprint. Discussion started: 19 October 2026
© Author(s) 2026. CC BY 4.0 License.

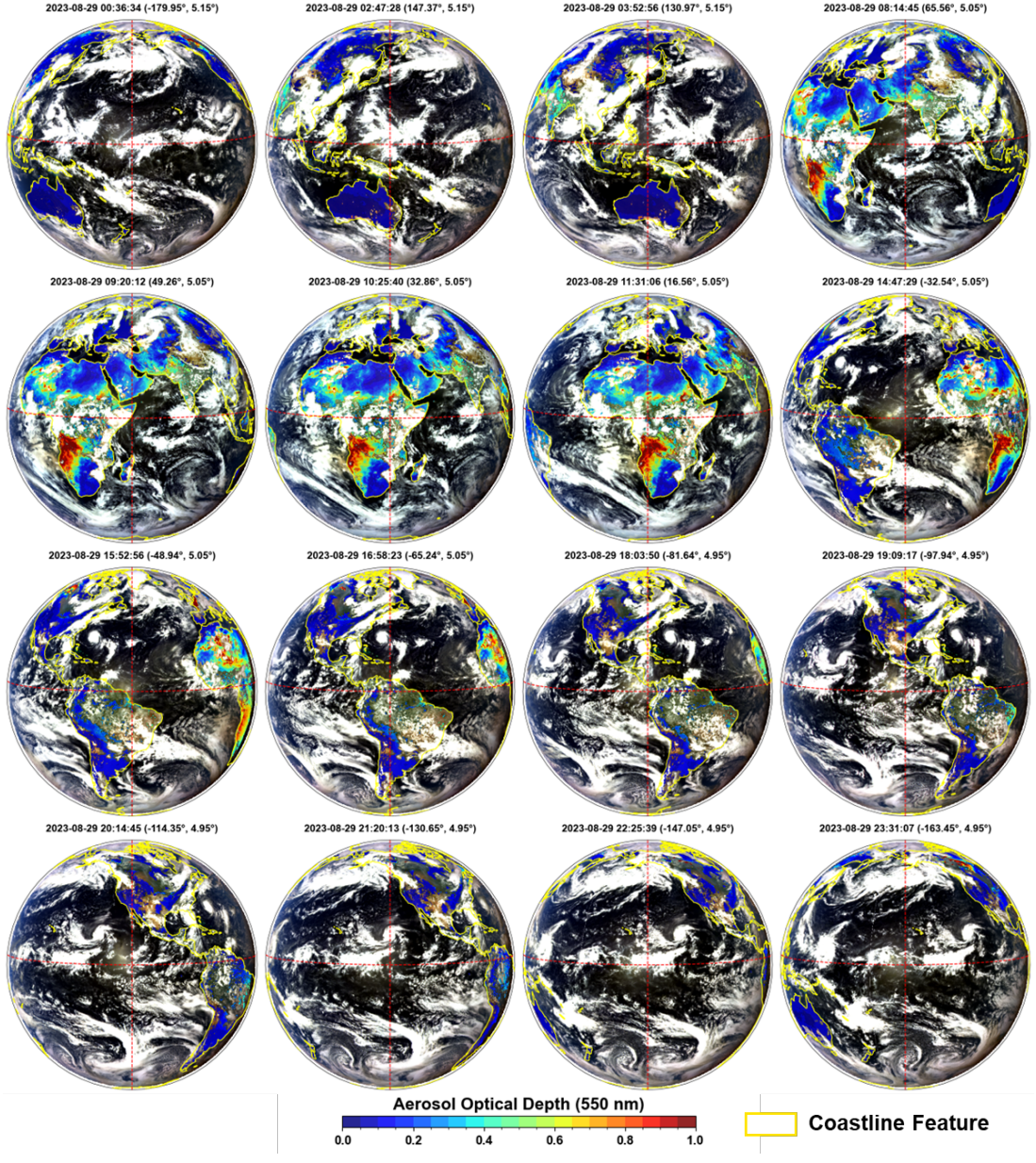


Figure 4. Continuous diurnal evolution of global AOD at 550 nm across the sunlit Earth disk on 29 August 2023. The 16 sequential orthographic projections display the retrieved AOD on the corresponding DSCOVR EPIC true-color RGB composite images. The acquisition time and satellite coordinates (longitude and latitude) are indicated above each panel.

https://doi.org/10.5194/egusphere-2026-5788
Preprint. Discussion started: 19 October 2026
© Author(s) 2026. CC BY 4.0 License.

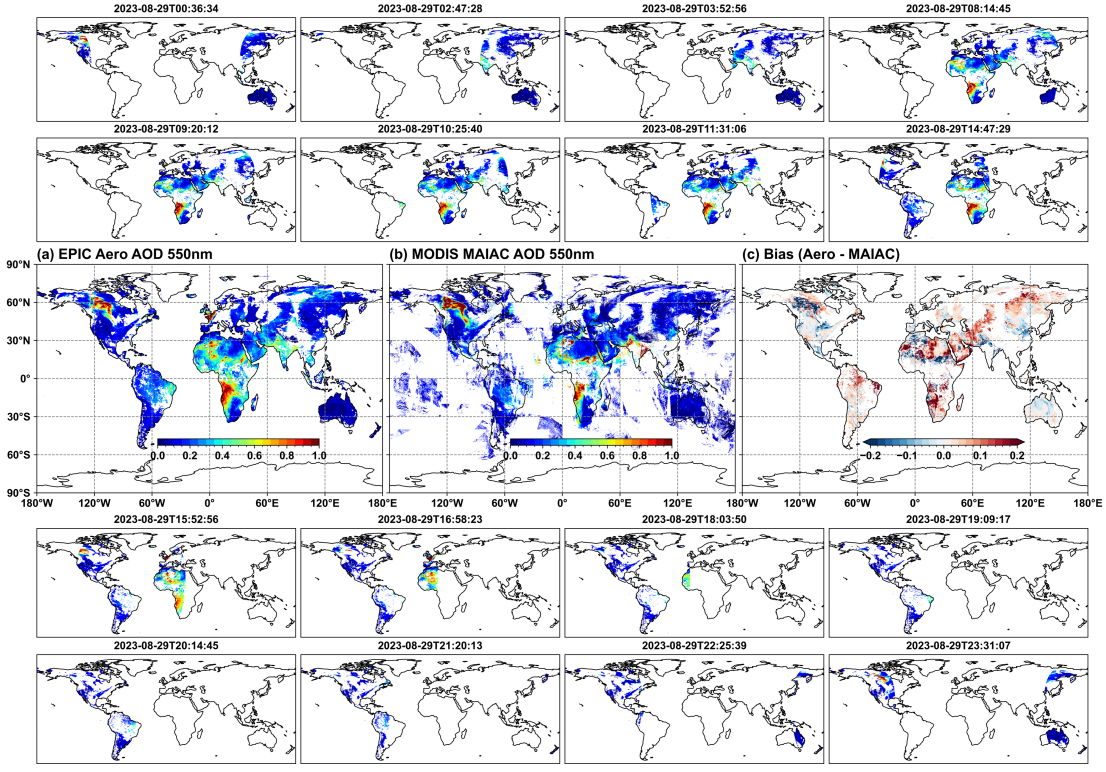


Figure 5. Global spatial patterns and high-frequency diurnal variability of AOD (550 nm) on 29 August 2023. The main panels compare the daily AOD: (a) daily AOD retrieved from EPIC; (b) the corresponding daily AOD from MODIS MAIAC; (c) the spatial distribution of the retrieval differences (EPIC − MAIAC). The sequences of smaller subpanels at the top and bottom illustrate the hourly evolution of AOD across the sunlit disk.

4.4 Analysis of Retrieval Error and Uncertainty

As shown in Fig. 6, the retrieval demonstrates high accuracy across global site-based validations. For most sites, the fraction of retrievals within the expected error envelope (InEE) exceeds 80%, the GCOS compliance rate exceeds 50%, the correlation coefficient (R) is above 0.8, and the overall error remains low (MAE < 0.06, RMSE < 0.08). Only in parts of Central Africa and East Asia does the RMSE locally increase to approximately 0.12. In the spatial extrapolation assessment (Fig. S2, S4), although overall error increases slightly as expected, these higher errors are concentrated mainly in regions such as India (IND), North America / Middle East (NAME), and Southeast Asia (SEA), with RMSE reaching ~0.2 and retrieval uncertainty increasing to ~0.06. This is primarily attributed to extraordinarily high aerosol loadings in these regions and the complex mixture of anthropogenic pollution and natural dust. Similarly, temporal extrapolation results (Fig. S3) confirm the robustness of the algorithm under strong seasonal variability. Furthermore, cross-year temporal independence validation (Table S1) demonstrates high temporal stability (2020: R = 0.790, InEE = 81.03%; 2023: R = 0.700, InEE = 78.09%), with MAE consistently around 0.05 or 0.06.

https://doi.org/10.5194/egusphere-2026-5788
Preprint. Discussion started: 19 October 2026
© Author(s) 2026. CC BY 4.0 License.

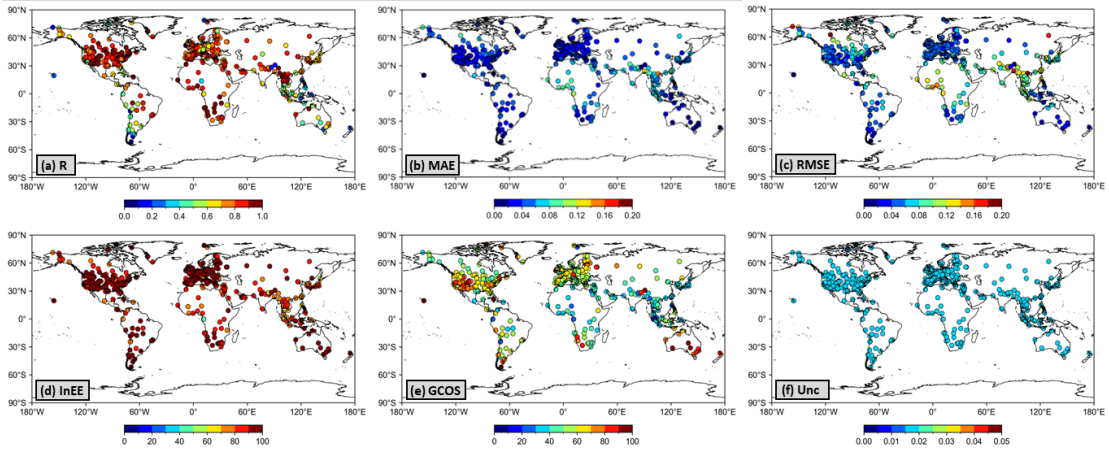


Figure 6. Global spatial distribution of validation metrics for retrieved AOD under a sample-based 10-fold cross-validation (10-CV) strategy. Metrics include (a) correlation coefficient (R), (b) mean absolute error (MAE), (c) root mean square error (RMSE), (d) fraction within expected error (InEE), (e) GCOS compliance rate, and (f) retrieval uncertainty (Unc).

Fig. 7 illustrates the error and uncertainty of AOD retrievals across various atmospheric and surface conditions. As shown in Fig. 7a, retrieval error varies significantly with aerosol loading. Under low AOD conditions (< 0.4), retrieval error is low (MAE < 0.1, RMSE < 0.1). As AOD increases (0.4 ≤ AOD < 1), bias shifts positively, indicating systematic overestimation. Under high AOD conditions (≥ 1), the interquartile range of errors becomes significantly wider. This pattern demonstrates that severe pollution is the primary source of uncertainty in the current algorithm. In addition to the long-tailed data distribution (e.g., 141,281 samples in the 0-0.1 range vs. 99 samples with AOD > 2.0), training imbalance and radiative transfer saturation under optically thick conditions also contribute to errors. In contrast to aerosol loading, the model shows strong stability across different particle sizes. Fig. 7b shows that the retrieval bias, MAE, and RMSE remain stable across a wide AE range, with bias close to zero. For the mixed fine-coarse modes, results are highly stable (MAE ~0.05, RMSE ~0.07). Under extreme conditions, coarse-mode dominance (AE < 0.5) is underestimated, while pure fine-mode aerosols (AE > 2.0) are overestimated. Furthermore, the model maintains high stability across varying surface conditions. As shown in Fig. 7c, MAE and RMSE remain nearly constant (~0.05 and ~0.07, respectively) across NDVI values ranging from bare soil (~0.1) to dense vegetation (~0.9), demonstrating strong robustness to surface heterogeneity. This may be attributed to the stable scattering geometry of EPIC observations and the advantages of the ensemble model.

https://doi.org/10.5194/egusphere-2026-5788
Preprint. Discussion started: 19 October 2026
© Author(s) 2026. CC BY 4.0 License.

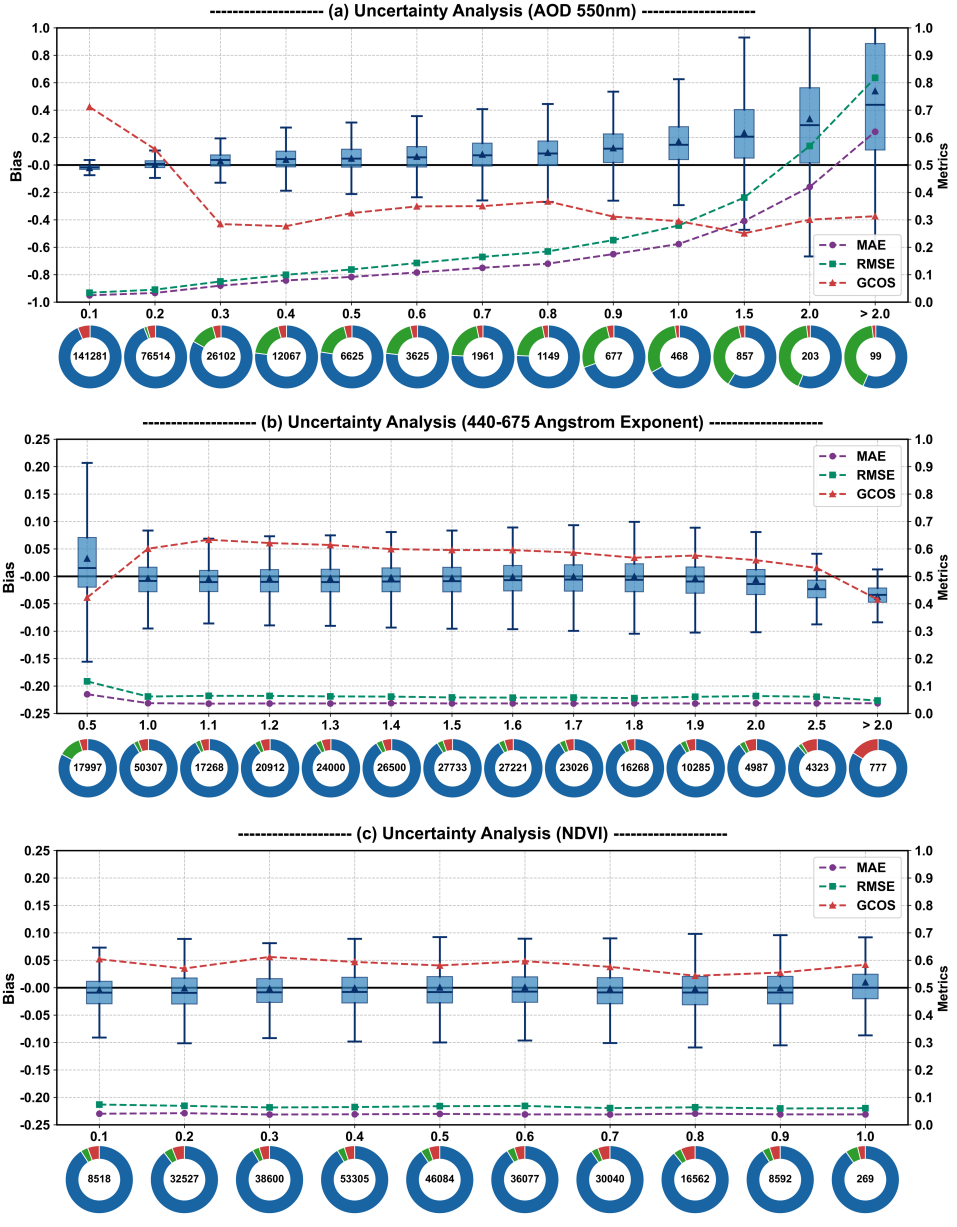


Figure 7. Uncertainty analysis of the retrieved AOD against AEROENT measurements as a function of (a) AOD at 550 nm, (b) Angstrom Exponent (440–675 nm), and (c) NDVI (from MODIS products). The box plot presents the bias (left y-axis), the central solid line marks the median, the triangle symbol represents the mean value, the box boundaries indicate the interquartile range (25th and 75th percentiles), and the whiskers represent the 1.5 interquartile range. The dashed lines corresponding to the right y-axis shows the Mean Absolute Error (purple), Root Mean Square Error (green), and the fraction of retrievals falling within the GCOS requirement (red). The pie charts at the bottom of each panel illustrate the sample size and the proportion of retrievals that are within the expected error envelope (blue), overestimated (red), and underestimated (green) for each specific bin.

https://doi.org/10.5194/egusphere-2026-5788
Preprint. Discussion started: 19 October 2026
© Author(s) 2026. CC BY 4.0 License.

5. Dynamic monitoring application of wildfire events

Extreme wildfire events are characterized by intense short-term emissions and rapid transport processes; however, LEO satellites (e.g., MODIS and VIIRS, with only 1–2 overpasses daily) cannot fully resolve their sub-diurnal variability. This section demonstrates the application of the proposed framework to dynamically monitor three representative wildfire events. The first case focuses on the 2023 Canadian wildfires, where high latitude conditions combined with dense smoke caused extensive data loss in cloud mask, severely limiting their downstream utility. The second case examines the 2023 Australian wildfires, where abundant valid observations enabled a more complete characterization of smoke evolution. The final case investigates the 2020 western U.S. wildfires, where the retrievals captured the long-range transcontinental transport of wildfire aerosols. For visualization clarity, the displayed AOD values are stretched to the range of 0-1. This stretching is applied to enhance the visualization of smoke distribution.

5.1 The Canadian wildfires of 2023

Fig. 8 illustrates the intraday variations in retrieved AOD at a ~1–2 h temporal resolution during the severe Canadian wildfire event on 11 July 2023. The results successfully capture the transport trajectory of aerosol plumes spreading outward from dense fire source regions, and the spatial structure of high AOD areas (>1.0, dark red) closely matches the geometry of the smoke plume. Comparison with EPIC Aero AOD (daily mean) and the widely used MODIS MAIAC AOD product (Fig. S6), overlaid with wind fields, shows that the proposed retrievals are highly consistent with MAIAC in terms of spatial patterns. Both products accurately depict a high-concentration smoke transport corridor across central and western Canada. Owing to EPIC's high frequency observations, its daily mean product provides more complete spatial coverage in regions where LEO satellites are hindered by cloud contamination during overpasses (white gaps in Fig. S6b). However, overall EPIC AOD values remain lower than those from MAIAC, likely due to the underestimation of peak AOD values and temporal averaging effects. Additionally, true-color imagery indicates that the official cloud mask products may over-mask heavy smoke, thereby affecting continuous monitoring of wildfire emissions.

https://doi.org/10.5194/egusphere-2026-5788
Preprint. Discussion started: 19 October 2026
© Author(s) 2026. CC BY 4.0 License.

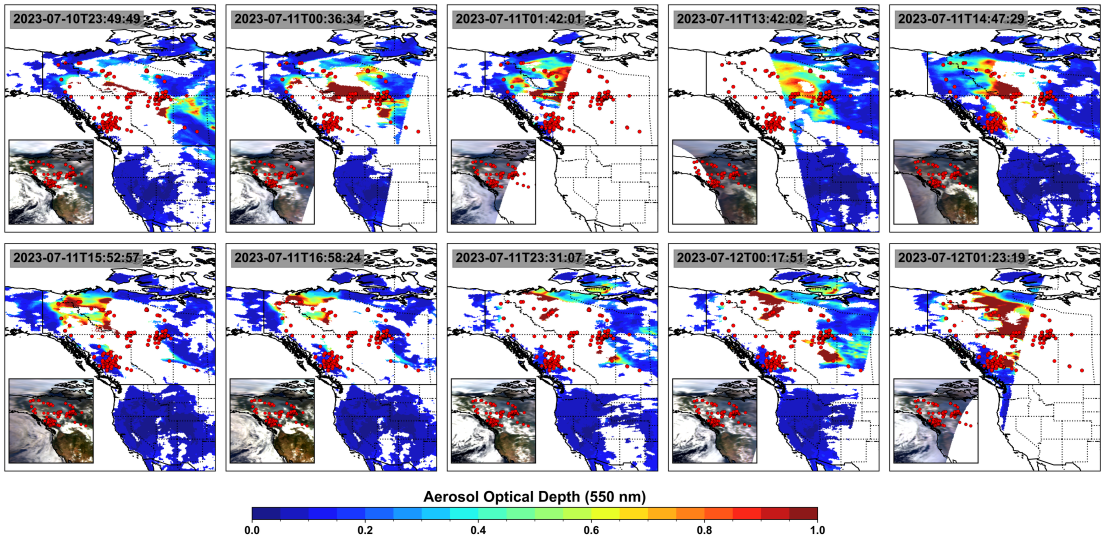


Figure 8. Sub-diurnal evolution of Aerosol Optical Depth (550 nm) retrieved from DSCOVR EPIC during the severe Canadian wildfire event on 11 July 2023. Solid red dots denote active fire hotspots detected by the MODIS Fire Information for Resource Management System (FIRMS). The lower-left inset in each panel shows the corresponding EPIC true-color RGB composite image, providing visual context for smoke plumes and cloud cover.

5.2 The Australian wildfires of 2023

A second case study focuses on the northern Australian wildfires, which exhibit pronounced persistence and clear diurnal variability. Fig. 9 shows sub-diurnal AOD variations for selected dates from 21 to 28 October, with five observations daily. The time series underscores the persistent nature of wildfire emissions. Driven by diurnal surface heating and boundary layer turbulence, high AOD regions (AOD > 0.6) exhibit a clear daily cycle, expanding during the morning and gradually dissipating toward evening (left to right columns) (Fan et al., 2025; Kuang et al., 2015). Furthermore, zoomed in subpanels of the fire intensive region (red bounding boxes) demonstrate that the retrievals capture fine spatial gradient variations near emission sources. Over the 10-day continuous period (Fig. S7), the proposed retrievals significantly improve data availability by reducing data gaps caused by orbital swaths and cloud contamination compared with MODIS MAIAC. Crucially, they maintain strong spatial consistency with MAIAC regarding overall distribution patterns and high-AOD centers.

https://doi.org/10.5194/egusphere-2026-5788
Preprint. Discussion started: 19 October 2026
© Author(s) 2026. CC BY 4.0 License.

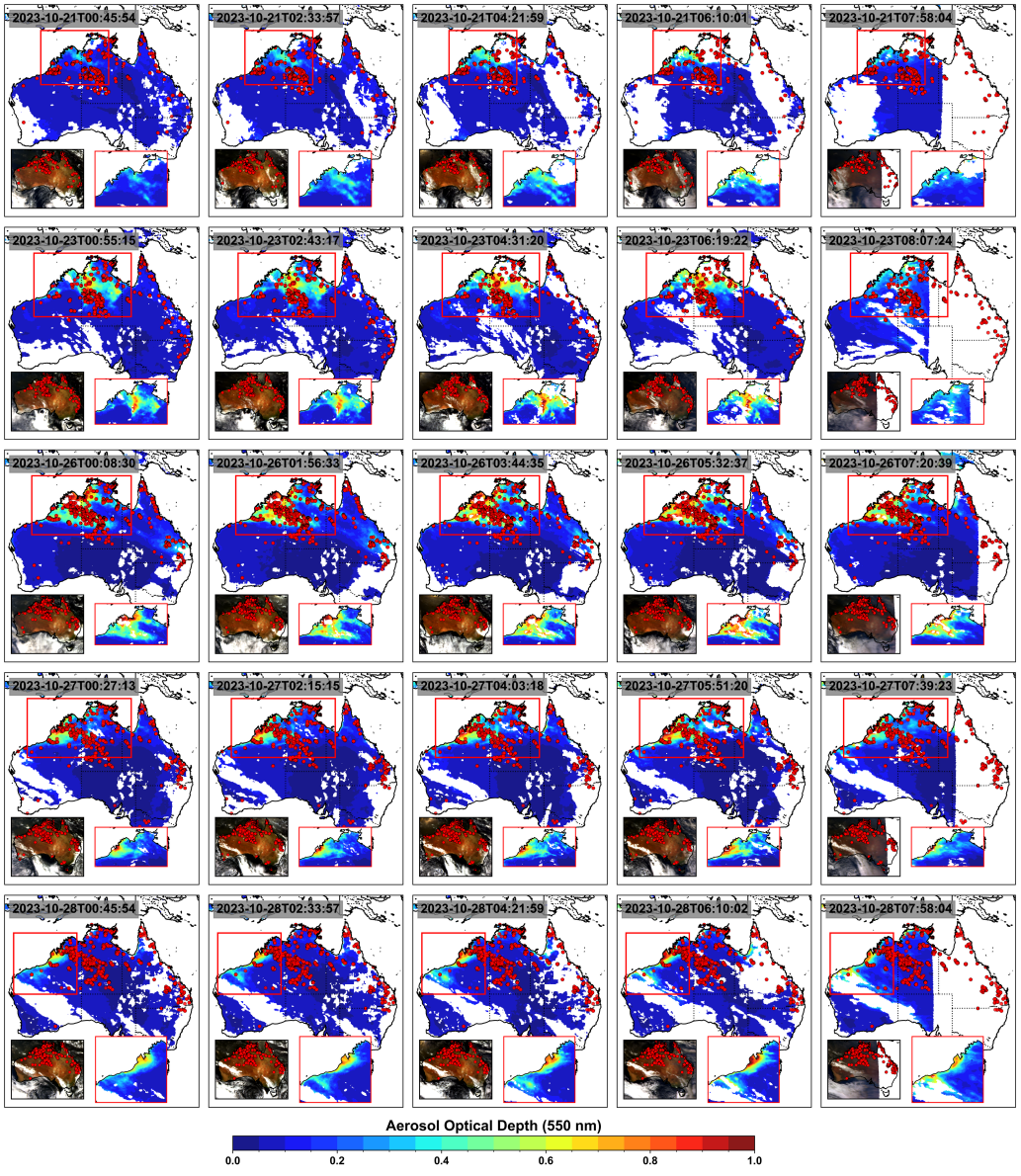


Figure 9. Multi-day diurnal evolution of Aerosol Optical Depth (550 nm) during the prolonged northern Australian wildfires from 21 to 28 October 2023. Each row represents a selected day with five observations per day. Solid red dots indicate active fire hotspots detected by MODIS FIRMS. For each panel, the lower-left inset shows the corresponding EPIC true-color RGB image, while the lower-right inset shows a magnified view of AOD distribution within the core fire region (outlined by the red bounding box).

5.3 The west U.S. wildfires of 2020

Fig. 10 presents a detailed characterization of the large-scale biomass-burning aerosol emissions from the extreme western U.S. wildfires in September 2020. As shown in the left panels (10–14 September), dense fire hotspots (red dots) along the U.S. West Coast (California, Oregon, and Washington) produced intense smoke plumes (AOD > 1.0) (Lu et al., 2021). Driven by

https://doi.org/10.5194/egusphere-2026-5788
Preprint. Discussion started: 19 October 2026
© Author(s) 2026. CC BY 4.0 License.

strong mid-latitude westerlies, the aerosol plume was transported eastward across the North American continent (Filonchyk et al., 2022; Suo et al., 2025) Notably, on 11–12 September, an anomalously high AOD region emerged over western Europe, particularly the United Kingdom, France, and surrounding areas. Given the sparse distribution of local fire hotspots, this aerosol anomaly cannot be attributed to local emissions. Trajectory analysis based on CAMS by ECMWF (2020) confirms that the high concentration aerosol plume originated from western U.S. wildfire smoke and was transported across the Atlantic Ocean over several days before reaching Europe (Ceamanos et al., 2023b). This provides direct observational evidence that extreme regional fire emissions can substantially affect hemispheric scale air quality. More importantly, the right subpanels of Fig. 10, focusing on the high AOD region over Europe, demonstrate the capability of the retrieval method to capture sub-diurnal aerosol plume evolution. Zooming in 11 September (green frame) and 12 September (red frame), hourly observations (1–2 h resolution) capture the spatiotemporal evolution of dense smoke plumes entering from the northwestern European coast and rapidly propagating eastward across the continent. These records of fast-moving pollution belts effectively compensate for the limitations of LEO satellites.

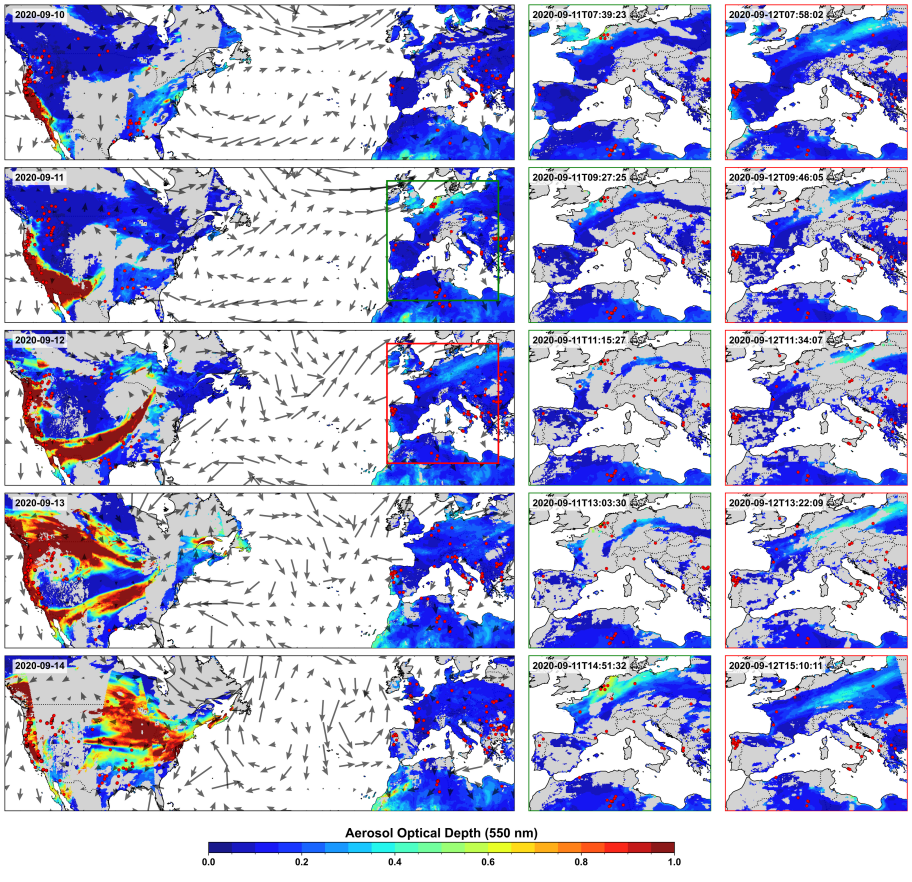


Figure 10. Spatiotemporal evolution of intercontinental transport of biomass-burning aerosols from the September 2020 western U.S. wildfires. The left panel shows daily mean AOD (550 nm) from 10–14 September, overlaid with active fire hotspots (red dots) and mean wind vectors (black arrows) from ECMWF ERA5 reanalysis. The right panels provide zoomed-in sub-daily views of anomalous aerosol plumes over Europe on 11 September (green boxes) and 12 September (red boxes).

https://doi.org/10.5194/egusphere-2026-5788
Preprint. Discussion started: 19 October 2026
© Author(s) 2026. CC BY 4.0 License.

6. Conclusions

In response to the need for persistent, large-scale monitoring of extreme wildfire aerosols, this study leverages the unique spatiotemporal capabilities of DSCOVR EPIC to develop an end-to-end deep learning retrieval framework. By integrating multispectral radiative signals, meteorological data, and topographic features, the proposed method effectively overcoming limitations of traditional physics-based algorithms, such as high computational cost and strong reliance on a priori assumptions, thereby achieving global sub-diurnal AOD retrieval from a single satellite platform.

Despite significant progress in high-frequency global aerosol retrievals, several limitations remain. First, the effective observation frequency of DSCOVR EPIC varies with season and latitude, yielding fewer than 10 daily observations at high latitudes. Furthermore, the current cloud mask product is prone to over-masking and occasionally misclassifying smoke plumes, leading to the loss of valuable observations in core wildfire regions (Fig. 4 and the Canadian wildfire case). Second, during complex and rapidly evolving wildfire events, aerosol characterization should not be limited to total column loading alone. In many combustion and long-range transport scenarios, AOD may not exhibit abrupt changes, whereas single-scattering albedo (SSA), which reflects aerosol composition and aging processes, can vary significantly. Accordingly, future research will focus on two directions. First, we aim to integrate EPIC with next-generation geostationary (GEO) satellites to enable synergistic observations at higher spatiotemporal resolutions. Second, the framework will be extended to retrieve additional optical parameters, enabling a more comprehensive characterization of aerosol scattering and absorption processes and providing better quantitative constraints for global radiative forcing assessments.

https://doi.org/10.5194/egusphere-2026-5788
Preprint. Discussion started: 19 October 2026
© Author(s) 2026. CC BY 4.0 License.

Data availability

The ground-based AOD measurements from AERONET is available at https://aeronet.gsfc.nasa.gov/. The DSCOVR/EPIC satellite data and corresponding cloud masks, UV-based AOD, and MAIAC-based AOD are available at https://www.earthdata.nasa.gov/data/. The reanalysis MERRA-2 data is available at https://gmao.gsfc.nasa.gov/. The ERA5 reanalysis data are available at https://cds.climate.copernicus.eu/. DEM is available at https://www.usgs.gov/coastal-changes-and-impacts/gmted2010. The active fire data from Fire Information for Resource Management System is available at https://firms.modaps.eosdis.nasa.gov/. The MODIS MAIAC aerosol product is available at https://ladsweb.modaps.eosdis.nasa.gov/.

Acknowledgements

This work was supported in part by the National Natural Science Foundation of China (NSFC) under Grant 42275147 and the Postgraduate Research & Practice Innovation Program of Jiangsu Province (Grant 26CXJH2389). Xiaohu Sun thanks for the joint Ph.D. program from China Scholarship Council (CSC) Grant No. 202509040059.

References

Ahn, C., Torres, O., Jethva, H., Tiruchirapalli, R., and Huang, L.: Evaluation of Aerosol Properties Observed by DSCOVR/EPIC Instrument From the Earth-Sun Lagrange 1 Orbit, J. Geophys. Res. Atmos., 126, e2020JD033651, https://doi.org/10.1029/2020JD033651, 2021.

Ansmann, A., Ohneiser, K., Mamouri, R.-E., Knopf, D. A., Veselovskii, I., Baars, H., Engelmann, R., Foth, A., Jimenez, C., Seifert, P., and Barja, B.: Tropospheric and stratospheric wildfire smoke profiling with lidar: mass, surface area, CCN, and INP retrieval, Atmos. Chem. Phys., 21, 9779–9807, https://doi.org/10.5194/acp-21-9779-2021, 2021.

CAMS: CAMS monitors smoke release from devastating US wildfires | Copernicus, https://atmosphere.copernicus.eu/cams-monitors-smoke-release-us-wildfires, last access: 26 July 2026, 2020.

Ceamanos, X., Six, B., Moparthy, S., Carrer, D., Georgeot, A., Gasteiger, J., Riedi, J., Attié, J.-L., Lyapustin, A., and Katsev, I.: Instantaneous aerosol and surface retrieval using satellites in geostationary orbit (iAERUS-GEO) – estimation of 15 min aerosol optical depth from MSG/SEVIRI and evaluation with reference data, Atmos. Meas. Tech., 16, 2575–2599, https://doi.org/10.5194/amt-16-2575-2023, 2023a.

Ceamanos, X., Coopman, Q., George, M., Riedi, J., Parrington, M., and Clerbaux, C.: Remote sensing and model analysis of biomass burning smoke transported across the Atlantic during the 2020 Western US wildfire season, Sci. Rep., 13, 16014, https://doi.org/10.1038/s41598-023-39312-1, 2023b.

Che, H., Xia, X., Zhao, H., Li, L., Gui, K., Zheng, Y., Song, J., Qi, B., Zhu, J., Miao, Y., Wang, Y., Wang, Z., Wang, H., Dubovik, O., Holben, B., Chen, H., Shi, G., and Zhang, X.: Aerosol optical and radiative properties and their environmental effects in China: A review, Earth-Sci. Rev., 248, 104634, https://doi.org/10.1016/j.earscirev.2023.104634, 2024.

https://doi.org/10.5194/egusphere-2026-5788
Preprint. Discussion started: 19 October 2026
© Author(s) 2026. CC BY 4.0 License.

Chen, X., Wang, J., Xu, X., Zhou, M., Zhang, H., Castro Garcia, L., Colarco, P. R., Janz, S. J., Yorks, J., McGill, M., Reid, J. S., de Graaf, M., and Kondragunta, S.: First retrieval of absorbing aerosol height over dark target using TROPOMI oxygen B band: Algorithm development and application for surface particulate matter estimates, Remote Sens. Environ., 265, 112674, https://doi.org/10.1016/j.rse.2021.112674, 2021.

Deng, W., Wang, J., Zhou, M., Chen, X., Wu, X., Zhang, H., Cohen, J. B., Wei, J., Da Silva, A., Brasseur, G. P., Granier, C., and Rouil, L.: Fires reverse progress toward ozone air quality standards in the United States, Science, 392, 1088–1092, https://doi.org/10.1126/science.aed3197, 2026.

Dubovik, O. and King, M. D.: A flexible inversion algorithm for retrieval of aerosol optical properties from Sun and sky radiance measurements, J. Geophys. Res. Atmos., 105, 20673–20696, https://doi.org/10.1029/2000JD900282, 2000.

Fan, K., Zhang, M., Li, H., Wang, L., Yang, X., and Kong, X.: Study on Global Aerosol Direct Radiative Effect by Fast Calculation Methods for Satellite Observations, IEEE Trans. Geosci. Remote Sens., 63, 1–17, https://doi.org/10.1109/TGRS.2025.3609397, 2025a.

Fan, Y., Sun, L., Wang, Z., Pang, S., and Wei, J.: Unveiling diurnal aerosol layer height variability from space using deep learning, ISPRS J. Photogramm. Remote Sens., 229, 211–222, https://doi.org/10.1016/j.isprsjprs.2025.08.021, 2025b.

Fan, Y., Li, Z., Sun, L., Dubovik, O., Wang, Z., Cheng, F., Shi, X., and Wei, J.: AeroTrans: Hourly AOD retrieval over land from MSG-1/SEVIRI imagery integrating Transformer and transfer learning, Remote Sens. Environ., 335, 115268, https://doi.org/10.1016/j.rse.2026.115268, 2026.

Filonchyk, M., Peterson, M. P., and Sun, D.: Deterioration of air quality associated with the 2020 US wildfires, Sci. Total Environ., 826, 154103, https://doi.org/10.1016/j.scitotenv.2022.154103, 2022.

Gandham, H., Dasari, H. P., Saharwardi, M. S., Karumuri, A., and Hoteit, I.: Dust sources over the Arabian Peninsula, Environ. Res. Lett., 18, 094053, https://doi.org/10.1088/1748-9326/acf388, 2023.

Giles, D. M., Sinyuk, A., Sorokin, M. G., Schafer, J. S., Smirnov, A., Slutsker, I., Eck, T. F., Holben, B. N., Lewis, J. R., Campbell, J. R., Welton, E. J., Korkin, S. V., and Lyapustin, A. I.: Advancements in the Aerosol Robotic Network (AERONET) Version 3 database – automated near-real-time quality control algorithm with improved cloud screening for Sun photometer aerosol optical depth (AOD) measurements, Atmos. Meas. Tech., 12, 169–209, https://doi.org/10.5194/amt-12-169-2019, 2019.

Gorishniy, Y., Kotelnikov, A., and Babenko, A.: TabM: Advancing Tabular Deep Learning with Parameter-Efficient Ensembling, https://doi.org/10.48550/arXiv.2410.24210, 18 February 2025., 2025.

de Graaf, M., Sneep, M., ter Linden, M., Tilstra, L. G., Donovan, D. P., van Zadelhoff, G.-J., and Veefkind, J. P.: Improvements in aerosol layer height retrievals from TROPOMI oxygen A-band measurements by surface albedo fitting in optimal estimation, Atmos. Meas. Tech., 18, 2553–2571, https://doi.org/10.5194/amt-18-2553-2025, 2025.

Holben, B. N., Eck, T. F., Slutsker, I., Tanré, D., Buis, J. P., Setzer, A., Vermote, E., Reagan, J. A., Kaufman, Y. J., Nakajima, T., Lavenu, F., Jankowiak, I., and Smirnov, A.: AERONET—A Federated Instrument Network and Data Archive for Aerosol Characterization, Remote Sens. Environ., 66, 1–16, https://doi.org/10.1016/S0034-4257(98)00031-5, 1998.

Hsu, N. C., Lee, J., Sayer, A. M., Kim, W., Bettenhausen, C., and Tsay, S. -C.: VIIRS Deep Blue Aerosol Products Over Land: Extending the EOS Long-Term Aerosol Data Records, J. Geophys. Res. Atmos., 124, 4026–4053, https://doi.org/10.1029/2018JD029688, 2019.

Ichii, X. L., Misaki Hase, Xuanlong Ma, Yuhei Yamamoto, Kazuhito: Geostationary Satellite Applications Expand into Land

https://doi.org/10.5194/egusphere-2026-5788
Preprint. Discussion started: 19 October 2026
© Author(s) 2026. CC BY 4.0 License.

Monitoring, https://eos.org/science-updates/geostationary-satellite-applications-expand-into-land-monitoring (last access: 2 July 2026), 2026., 2026.

Kim, H., Chen, X., Wang, J., Lu, Z., Zhou, M., Carmichael, G. R., Park, S. S., and Kim, J.: Aerosol layer height (ALH) retrievals from oxygen absorption bands: intercomparison and validation among different satellite platforms, GEMS, EPIC, and TROPOMI, Atmos. Meas. Tech., 18, 327–349, https://doi.org/10.5194/amt-18-327-2025, 2025.

Kuang, Y., Zhao, C. S., Tao, J. C., and Ma, N.: Diurnal variations of aerosol optical properties in the North China Plain and their influences on the estimates of direct aerosol radiative effect, Atmos. Chem. Phys., 15, 5761–5772, https://doi.org/10.5194/acp-15-5761-2015, 2015.

Levy, R. C., Remer, L. A., Kleidman, R. G., Mattoo, S., Ichoku, C., Kahn, R., and Eck, T. F.: Global evaluation of the Collection 5 MODIS dark-target aerosol products over land, Atmos. Chem. Phys., 10, 10399–10420, https://doi.org/10.5194/acp-10-10399-2010, 2010.

Levy, R. C., Mattoo, S., Munchak, L. A., Remer, L. A., Sayer, A. M., Patadia, F., and Hsu, N. C.: The Collection 6 MODIS aerosol products over land and ocean, Atmos. Meas. Tech., 6, 2989–3034, https://doi.org/10.5194/amt-6-2989-2013, 2013.

Li, F., Zhang, X., and Kondragunta, S.: Highly anomalous fire emissions from the 2019–2020 Australian bushfires, Environ. Res. Commun., 3, 105005, https://doi.org/10.1088/2515-7620/ac2e6f, 2021.

Li, P., Xue, Y., Dionisi, D., He, B., Wang, P., and Li, H.: Detecting the layer height of smoke and dust aerosols over land and ocean using ultraviolet dual-wavelength measurements, Remote Sens. Environ., 331, 115001, https://doi.org/10.1016/j.rse.2025.115001, 2025.

Lu, Z., Wang, J., Xu, X., Chen, X., Kondragunta, S., Torres, O., Wilcox, E. M., and Zeng, J.: Hourly Mapping of the Layer Height of Thick Smoke Plumes Over the Western U.S. in 2020 Severe Fire Season, Front. Remote Sens., 2, 766628, https://doi.org/10.3389/frsen.2021.766628, 2021.

Lu, Z., Wang, J., Chen, X., Zeng, J., Wang, Y., Xu, X., Christian, K. E., Yorks, J. E., Nowottnick, E. P., Reid, J. S., and Xian, P.: First Mapping of Monthly and Diurnal Climatology of Saharan Dust Layer Height Over the Atlantic Ocean From EPIC/DSCOVR in Deep Space, Geophys. Res. Lett., 50, e2022GL102552, https://doi.org/10.1029/2022GL102552, 2023.

Lyapustin, A., Wang, Y., Laszlo, I., Kahn, R., Korkin, S., Remer, L., Levy, R., and Reid, J. S.: Multiangle implementation of atmospheric correction (MAIAC): 2. Aerosol algorithm, J. Geophys. Res. Atmos., 116, https://doi.org/10.1029/2010JD014986, 2011.

Lyapustin, A., Wang, Y., Go, S., Choi, M., Korkin, S., Huang, D., Knyazikhin, Y., Blank, K., and Marshak, A.: Atmospheric Correction of DSCOVR EPIC: Version 2 MAIAC Algorithm, Front. Remote Sens., 2, 748362, https://doi.org/10.3389/frsen.2021.748362, 2021a.

Lyapustin, A., Go, S., Korkin, S., Wang, Y., Torres, O., Jethva, H., and Marshak, A.: Retrievals of Aerosol Optical Depth and Spectral Absorption From DSCOVR EPIC, Front. Remote Sens., 2, 645794, https://doi.org/10.3389/frsen.2021.645794, 2021b.

Lyapustin, A., Choi, M., Wang, Y., Korkin, S., Hyer, E., and Marshak, A.: Simultaneous retrieval of aerosol optical depth, spectral absorption and layer height from DSCOVR EPIC using MAIAC algorithm, Front. Remote Sens., 6, https://doi.org/10.3389/frsen.2025.1677438, 2025.

Marshak, A., Herman, J., Adam, S., Karin, B., Carn, S., Cede, A., Geogdzhayev, I., Huang, D., Huang, L.-K., Knyazikhin, Y., Kowalewski, M., Krotkov, N., Lyapustin, A., McPeters, R., Meyer, K. G., Torres, O., and Yang, Y.: Earth Observations from

https://doi.org/10.5194/egusphere-2026-5788
Preprint. Discussion started: 19 October 2026
© Author(s) 2026. CC BY 4.0 License.

DSCOVR EPIC Instrument, Bull. Am. Meteorol. Soc., 99, 1829–1850, https://doi.org/10.1175/BAMS-D-17-0223.1, 2018.

Mhawish, A., Banerjee, T., Sorek-Hamer, M., Lyapustin, A., Broday, D. M., and Chatfield, R.: Comparison and evaluation of MODIS Multi-angle Implementation of Atmospheric Correction (MAIAC) aerosol product over South Asia, Remote Sens. Environ., 224, 12–28, https://doi.org/10.1016/j.rse.2019.01.033, 2019.

Qin, W., Fang, H., Wang, L., Wei, J., Zhang, M., Su, X., Bilal, M., and Liang, X.: MODIS high-resolution MAIAC aerosol product: Global validation and analysis, Atmos. Environ., 264, 118684, https://doi.org/10.1016/j.atmosenv.2021.118684, 2021.

Qu, J., Holzmüller, D., Varoquaux, G., and Morvan, M. L.: TabICLv2: A better, faster, scalable, and open tabular foundation model, https://doi.org/10.48550/arXiv.2602.11139, 11 February 2026., 2026.

Rizkallah, L. W.: Enhancing the performance of gradient boosting trees on regression problems, J. Big Data, 12, 35, https://doi.org/10.1186/s40537-025-01071-3, 2025.

Sasi, S., Natraj, V., Molina García, V., Efremenko, D. S., Loyola, D., and Doicu, A.: Model Selection in Atmospheric Remote Sensing with an Application to Aerosol Retrieval from DSCOVR/EPIC, Part 1: Theory, Remote Sens., 12, 3724, https://doi.org/10.3390/rs12223724, 2020.

Sawyer, V., Levy, R. C., Mattoo, S., Shi, Y. R., Kim, M., Remer, L. A. A., and Cureton, G. P.: An updated VIIRS dark target aerosol product for continuity with MODIS: assessing regional aerosol trends, Front. Environ. Sci., 13, https://doi.org/10.3389/fenvs.2025.1602145, 2025.

Sayer, A. M., Munchak, L. A., Hsu, N. C., Levy, R. C., Bettenhausen, C., and Jeong, M. -J.: MODIS Collection 6 aerosol products: Comparison between Aqua's e-Deep Blue, Dark Target, and "merged" data sets, and usage recommendations, J. Geophys. Res. Atmos., 119, https://doi.org/10.1002/2014JD022453, 2014.

Sun, X., Xue, Y., and Sun, L.: Enhancing global aerosol retrieval from satellite data via deep learning with mutual information estimation, Int. J. Appl. Earth Obs. Geoinformation, 139, 104534, https://doi.org/10.1016/j.jag.2025.104534, 2025.

Sun, X., Xue, Y., Kanniah, K. D., and Cui, Z.: Multi-Parameter Aerosol Retrieval From Landsat Data Under Small Dataset Constraints, IEEE Trans. Geosci. Remote Sens., 64, 1–11, https://doi.org/10.1109/TGRS.2025.3646650, 2026.

Suo, Z., Wang, Q., Lu, Y., Yao, Y., Song, Q., Ding, J., Ju, W., and Zhang, Z.: Satellite-borne identification and quantification of wildfire smoke emissions in North America via a novel UV-based index, Atmos. Environ., 346, 121069, https://doi.org/10.1016/j.atmosenv.2025.121069, 2025.

Tian, X., Gao, L., Li, C., and Li, J.: Retrieving High Temporal Resolution Aerosol Layer Height From EPIC/DSCOVR Using Machine Learning Method, IEEE Trans. Geosci. Remote Sens., 62, 1–11, https://doi.org/10.1109/TGRS.2024.3405186, 2024.

Tindan, J. Z., Pu, B., and Jin, Q.: Trends in daytime and nighttime dust aerosols over the Dust Belt revealed by IASI, Sci. Total Environ., 1004, 180742, https://doi.org/10.1016/j.scitotenv.2025.180742, 2025.

Torres, O. and Ahn, C.: Local and Regional Diurnal Variability of Aerosol Properties Retrieved by DSCOVR/EPIC UV Algorithm, J. Geophys. Res. Atmos., 129, e2023JD039908, https://doi.org/10.1029/2023JD039908, 2024.

Torres, O., Jethva, H., Ahn, C., and Kayetha, V.: A decade of global hourly aerosol observations from DSCOVR/EPIC using near-UV measurements, Front. Remote Sens., 6, https://doi.org/10.3389/frsen.2025.1685415, 2025.

Wang, H., Maslanka, W., Palmer, P. I., Wooster, M. J., Wang, H., Yao, F., Feng, L., Wu, K., Lu, X., and Fan, S.: Using

https://doi.org/10.5194/egusphere-2026-5788
Preprint. Discussion started: 19 October 2026
© Author(s) 2026. CC BY 4.0 License.

geostationary-satellite-derived sub-daily fire radiative power variability versus prescribed diurnal cycles to assess the impact of African fires on tropospheric ozone, Atmos. Chem. Phys., 25, 17501–17526, https://doi.org/10.5194/acp-25-17501-2025, 2025.

Wang, L., Su, X., Wang, Y., Cao, M., Lang, Q., Li, H., Sun, J., Zhang, M., Qin, W., Li, L., and Yang, L.: Towards long-term, high-accuracy, and continuous satellite total and fine-mode aerosol records: Enhanced Land General Aerosol (e-LaGA) retrieval algorithm for VIIRS, ISPRS J. Photogramm. Remote Sens., 214, 261–281, https://doi.org/10.1016/j.isprsjprs.2024.06.022, 2024.

Wei, J., Li, Z., Lyapustin, A., Wang, J., Dubovik, O., Schwartz, J., Sun, L., Li, C., Liu, S., and Zhu, T.: First close insight into global daily gapless 1 km PM2.5 pollution, variability, and health impact, Nat. Commun., 14, 8349, https://doi.org/10.1038/s41467-023-43862-3, 2023.

Wen, Y., Tran, D., and Ba, J.: BatchEnsemble: An Alternative Approach to Efficient Ensemble and Lifelong Learning, https://doi.org/10.48550/arXiv.2002.06715, 20 February 2020., 2020.

Xu, X., Wang, J., Wang, Y., Zeng, J., Torres, O., Yang, Y., Marshak, A., Reid, J., and Miller, S.: Passive remote sensing of altitude and optical depth of dust plumes using the oxygen A and B bands: First results from EPIC/DSCOVR at Lagrange-1 point, Geophys. Res. Lett., 44, 7544–7554, https://doi.org/10.1002/2017GL073939, 2017.

Xu, X., Wang, J., Wang, Y., Zeng, J., Torres, O., Reid, J. S., Miller, S. D., Martins, J. V., and Remer, L. A.: Detecting layer height of smoke aerosols over vegetated land and water surfaces via oxygen absorption bands: hourly results from EPIC/DSCOVR in deep space, Atmos. Meas. Tech., 12, 3269–3288, https://doi.org/10.5194/amt-12-3269-2019, 2019.

Yan, X., Chen, J., Chen, H. W., Zhang, Y., Jiang, Y., Wang, Q., Wang, G., Jia, K., Chen, Z., Dong, W., Fan, J., and Zhao, C.: Exploring Global Aerosol Size Dynamics from 2001 to 2024 Using the Pretrained Remote sensing pIxel-based Spatial-teMporal Deep Neural Network, Environ. Sci. Technol., 60, 7146–7158, https://doi.org/10.1021/acs.est.5c13469, 2026.

Yao, R., Shi, C., Letu, H., Yin, S., Nakajima, T., Sekiguchi, M., Xu, J., Rao, L., Wang, W., Tang, C., and Han, R.: A physics-based AI algorithm integrating radiative transfer and machine learning for joint retrieval of aerosol layer height and optical thickness from hyperspectral satellite observations over the ocean, Remote Sens. Environ., 338, 115379, https://doi.org/10.1016/j.rse.2026.115379, 2026.

Zhang, B., Zhang, Q., Wang, Z., and Yang, T.: Immediate remote sensing: Dynamic context-adaptive fusion for himawari-8/9 10-minute wildfire detection, Remote Sens. Environ., 344, 115524, https://doi.org/10.1016/j.rse.2026.115524, 2026.

Zhang, H., Hao, S., and Liu, C.: A Fast High-Precision Geospatial Grid Interpolation Algorithm, https://doi.org/10.21203/rs.3.rs-7812281/v1, 10 November 2025., 2025.